

Carbon Free and Noble Metal Free Ni₂Mo₆S₈ Electrocatalyst for Selective Electrosynthesis of H₂O₂

*Fan Xia, Bomin Li, Yiqi Liu, Yuzi Liu, Siyuan Gao, Ke Lu, Jacob Kaelin, Rongyue Wang, Tobin J. Marks, and Yingwen Cheng**

F. Xia, B. Li, S. Gao, K. Lu, J. Kaelin, Y. Cheng.

Department of Chemistry and Biochemistry, Northern Illinois University, DeKalb, IL 60115, United States

E-mail: ycheng@niu.edu

Y. Liu, T. J. Marks.

Department of Chemistry, Northwestern University, Evanston, Illinois, 60208, United States

Y. Liu.

Center for Nanoscale Materials, Argonne National Laboratory, Lemont, Illinois, 60439 United States.

B. Li, S. Gao, J. Kaelin, R. Wang.

Applied Materials Division, Argonne National Laboratory, Lemont, Illinois, 60439 United States

Keywords: selective electrocatalysis, oxygen reduction, hydrogen peroxide, earth abundant, carbon free

Electrocatalytic two-electron reduction of oxygen is highly promising for producing sustainable H₂O₂ but lacks low cost and selective electrocatalysts. Here, we present the Chevrel phase chalcogenide

This is the author manuscript accepted for publication and has undergone full peer review but has not been through the copyediting, typesetting, pagination and proofreading process, which may lead to differences between this version and the [Version of Record](#). Please cite this article as [doi: 10.1002/adfm.20204716](https://doi.org/10.1002/adfm.20204716).

This article is protected by copyright. All rights reserved.

$\text{Ni}_2\text{Mo}_6\text{S}_8$ as a novel active structure motif for reducing oxygen to H_2O_2 in aqueous electrolyte. Although has a low surface area, the $\text{Ni}_2\text{Mo}_6\text{S}_8$ catalyst exhibited exceptionally high activity for H_2O_2 synthesis with > 90% H_2O_2 molar selectivity across a wide potential range. Chemical titration verified successful generation of H_2O_2 and confirmed yielding rates as high as $90 \text{ mmol H}_2\text{O}_2 \text{ g}_{\text{cat}}^{-1}\text{h}^{-1}$. The outstanding activities were attributed to the ligand and ensemble effects of Ni on Mo_6S_8 that promote H_2O dissociation and proton-coupled reduction of O_2 to HOO^* , and the spatial effect of the Chevrel phase structure that isolate Ni active sites to inhibit O-O cleavage. The synergy of these effects delivered fast and selective production of H_2O_2 with high turn-over frequencies of $\sim 30 \text{ s}^{-1}$. In addition, the $\text{Ni}_2\text{Mo}_6\text{S}_8$ catalyst has stable crystal structure that is resistive for surface oxidation, and delivered good catalyst stability for continuous H_2O_2 production. The described new Ni- Mo_6S_8 active site motif could unlock new opportunities for designing advanced Earth-abundant electrocatalysts to tune oxygen reduction pathways for practical H_2O_2 production.

1. Introduction

Hydrogen peroxide (H_2O_2) is an important commodity chemical and has versatile applications in many areas, including chemical synthesis, textile manufacturing and healthcare disinfection.^[1] It is ecofriendly and only produces water when used as an oxidant, thus is expected to play key roles in the rapidly developing sustainable industries.^[2] The global H_2O_2 market reached $\sim \$ 1.61$ billion in 2019 and has grown significantly in recent years, especially due to rising demands from healthcare applications. Currently, commercial H_2O_2 is manufactured almost exclusively from the indirect anthraquinone oxidation process, which involves multi-step hydrogenation and oxidation of anthraquinone using Pd-based catalysts.^[3] This process is only profitable with centralized plants and suffers from intensive energy consumption and substantial organic wastes generation.^[4] In addition, the centralized production demands for costly infrastructures for transportation and storage of hazardous bulk H_2O_2 . These sustainability drawbacks have motivated interests on alternative H_2O_2 production methods.^[5] The direct synthesis from oxygen and hydrogen mixture gas is being considered as an alternative, but it still requires hydrogen gas and expensive noble metal catalysts, and it is also economically challenging to manage the potentially explosive H_2/O_2 mixtures.^[6] Therefore, developing strategies for more sustainable H_2O_2 production has been

This article is protected by copyright. All rights reserved.

an ongoing challenges, particularly on the scalable modules that have promises for decentralized and on demand H₂O₂ production at the point of use.^[7]

The direct H₂O₂ synthesis based on electrocatalytic oxygen reduction or water oxidation reactions recently emerged as a promising route for scalable H₂O₂ under ambient condition.^[8] Depending on the electrochemical setup, this can operate as either a galvanic cell for simultaneous generation of electricity and H₂O₂ or an electrolytic cell for converting renewable electricity into H₂O₂ from water and air.^[9] The synthesis via the two-electron (2e⁻) electrocatalytic oxygen reduction reaction (ORR) offers better tunability and has been under intensive study.^[10] Unfortunately, this reaction faces strong competition with the well-established four-electron (4e⁻) ORR and promoting the 2e⁻ pathway requires highly selective electrocatalysts.^[11] Currently, noble metal alloys such as Pt-Au, Pt-Hg and Pd-Hg are among the most active electrocatalysts and deliver > 98% selectivity towards H₂O₂.^[12] The inactive Hg sites in these alloys isolate active noble metal site for optimal binding of HOO* and suppressing cleavage of O-O, but the scarcity of noble metals and toxicity of Hg practically hinder their large-scale applications. Recently, promising results have been described with a plethora of defective carbon and heteroatom doped carbon electrocatalysts, with 2e⁻/4e⁻ ORR selectivity strongly correlates with heteroatom doping and local atomic structure of carbon motifs.^[13] However, such catalysts usually have very complicated surface composition and therefore the active sites responsible for selective H₂O₂ synthesis were often not clearly defined. In addition, further performance improvements can be challenging without sacrificing stability or activity.^[14] Recently, Earth-abundant metal chalcogenides such as CoS₂ and CoSe₂ have shown with great promises for the 2e⁻ ORR, and the high performance was attributed to the lattice chalcogenide anions that separate active metal sites and inhibit undesirable 4e⁻ ORR.^[15] Overall, despite of the great progresses with current electrocatalysts, high H₂O₂ selectivity usually associates with significant overpotentials and/or limited current densities,^[16] and it is still highly challenging to obtain non-noble metal based

This article is protected by copyright. All rights reserved.

electrocatalyst for precise H₂O₂ synthesis with simultaneous high reactivity and selectivity.^[17] The design of novel active site motifs using earth-abundant metals (such as Fe, Co, Mn) and better isolated active sites could allow further optimized oxygen bonding and enhanced electrochemical reduction activity and H₂O₂ selectivity.^[18]

Herein, we describe a new Ni-Mo₆S₈ active site motif based on the Chevrel phase chalcogenide Ni₂Mo₆S₈ for catalyzing the selective 2e⁻ ORR to H₂O₂ in aqueous electrolytes. The Chevrel phase is a unique family of chalcogenides and has versatile crystal structure with three-dimensional channels from interconnected Mo₆S₈ clusters (Figure 1). It exhibits outstanding properties for a plethora of energy applications such as superconductors and batteries.^[19] As an oxygen reduction electrocatalyst, the carbon free and noble metal free Ni₂Mo₆S₈ catalyst enabled nearly exclusive H₂O₂ production with up to 98% molar selectivity, which was verified from both rotating ring-disc electrode measurements and chemical titration using Ce(SO₄)₂. The outstanding activity was attributed to the ligand and ensemble effects of Ni and the spatial confinement effect of Ni, Mo and S in the active motif of the catalysts. The synergy of these three effects providing the Ni₂Mo₆S₈ catalyst with an impressive turn over frequency (TOF) of ~ 30 s⁻¹ for nearly exclusive H₂O₂ synthesis with yielding rates reaching ~ 90 mmol H₂O₂ g_{cat}⁻¹ h⁻¹. In addition, the Ni₂Mo₆S₈ catalyst is resistive to surface oxidation and exhibited good stability for at least 10 hours continuous H₂O₂ synthesis.

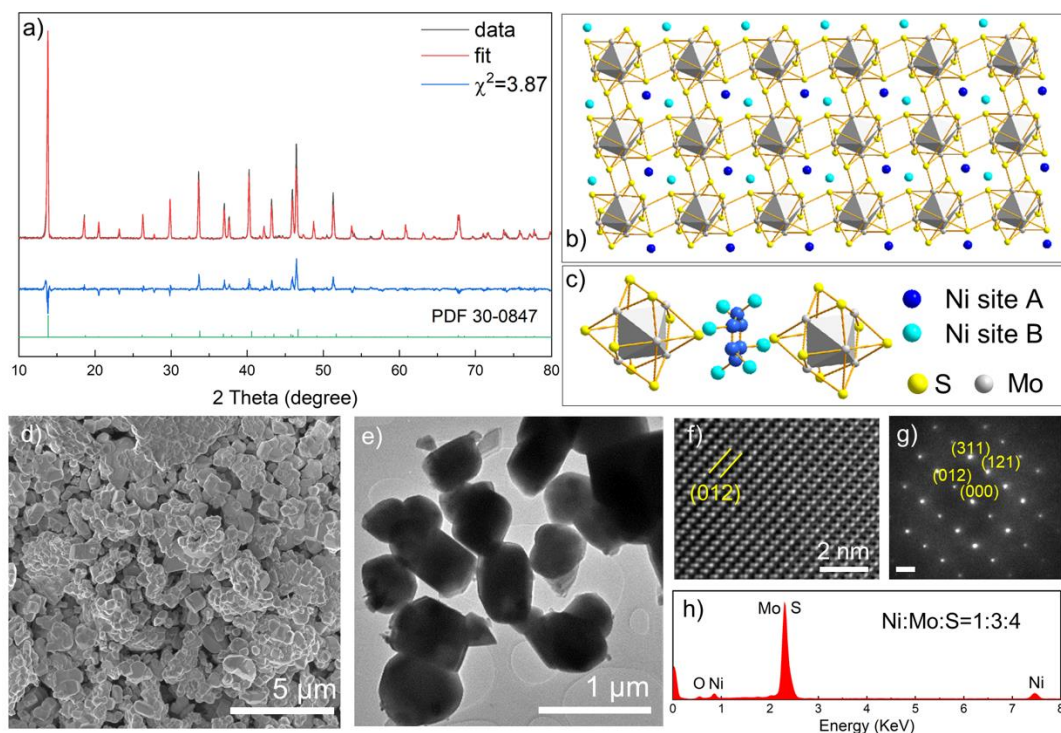


Figure 1: Structural characterization of the $\text{Ni}_2\text{Mo}_6\text{S}_8$ electrocatalysts: a) powder X-ray diffraction pattern and the Rietveld refinement results; b-c) schematic illustration of the crystal structure that shows interconnected Mo_6S_8 clusters and the two types of Ni sites around the trigonal axis; d) SEM; e-f) TEM images; g) selective area electron diffraction pattern (SAED) and h) energy-dispersive X-ray (EDX) spectrum.

2. Results and Discussion

The $\text{Ni}_2\text{Mo}_6\text{S}_8$ catalysts were synthesized using a two-step solid state method,^[20] starting from ball-milling of 0.57g NiS, 0.91g Mo and 1.50 g MoS_2 using a high energy mechanical miller and then calcinating the milled powder in a tube furnace under Ar at 1000°C for 10 hours. The powder X-ray diffraction (XRD) patterns of the produced $\text{Ni}_2\text{Mo}_6\text{S}_8$ catalyst match well with the rhombohedral R3H structure of the Chevrel phase (**Figure 1a**, PDF: 30-0847). The lattice parameters identified by Rietveld refinement are in good agreement with the literature (Table S1).^[19b, 21] Figure 1b illustrates the general crystal structure of $\text{Ni}_2\text{Mo}_6\text{S}_8$, which can be viewed as three-dimensional frameworks with interconnected Mo_6S_8 clusters, each having a Mo_6 octahedral surrounded by a S_8 cube. The Ni-ions distribute among sites A and B around the trigonal axis structured by Mo_6S_8 clusters (Figure 1c). The scanning (SEM) and transmission electron microscope (TEM) images revealed that the $\text{Ni}_2\text{Mo}_6\text{S}_8$ catalyst have relatively large particle size and a wide size distribution of 100 ~ 1000 nm, with quasi-

This article is protected by copyright. All rights reserved.

cubic morphology and rough surfaces (Figure 1d-e). The high-resolution TEM and selective area electron diffraction analysis revealed typical rhombohedral lattice spacing of the Chevrel phase chalcogenide (Figure 1f-g).^[22] The energy dispersive X-ray spectrum identified Ni, Mo and S as the principle elemental composition with atomic ratio of $\approx 1:3:4$. In addition, the nitrogen adsorption-desorption isotherm of the $\text{Ni}_2\text{Mo}_6\text{S}_8$ catalyst exhibited a Brunauer–Emmett–Teller (BET) specific surface area of $\sim 1 \text{ m}^2 \text{ g}^{-1}$ due to large particle size (Figure S1). For comparison, the Ni-free Mo_6S_8 catalyst was also prepared and studied to elucidate roles of Ni ions in $\text{Ni}_2\text{Mo}_6\text{S}_8$ on H_2O_2 selectivity. This catalyst was prepared by acid leaching of Ni^{2+} from $\text{Ni}_2\text{Mo}_6\text{S}_8$ and hence should have similar morphology and surface texture and its phase purity was confirmed by XRD (Figure S2).^[23]

The electrocatalytic oxygen reduction (ORR) can proceed via either a 2e^- pathway that converts H_2O_2 or a 4e^- pathway that converts to H_2O , and selectivity of these two pathways was mainly determined by the O-O bond cleavage kinetics on the electrocatalysts.^[15b, 24] The behavior of the $\text{Ni}_2\text{Mo}_6\text{S}_8$ catalyst on modulating the ORR pathway was studied using a standard three-electrode setup as detailed in the supplementary information. The reference electrode was a saturated calomel electrode (SCE) and its potential was calibrated as -0.998V vs. the reversible hydrogen electrode in 0.1M KOH (RHE, Figure S3). The voltages reported below are all converted in reference to the RHE. The working electrode was a rotating glassy carbon disc and Pt ring electrode (RRDE) and the ring collection efficiency was calibrated as 0.38 using the ferri-/ferrocyanide redox couple (Figure S4). The Pt ring electrode was set at 1.20 V vs. RHE during the ORR for selectively responding to H_2O_2 without interferences from the ORR and water oxidation reactions.^[15a] The catalyst ink was prepared using Nafion and was drop-casted on the disc electrode with areal loadings of $0.1 \sim 1.5 \text{ mg cm}^{-2}$. No carbon additive was used to avoid possible interferences in evaluating the true intrinsic activity of each catalyst.^[15a, 15b]

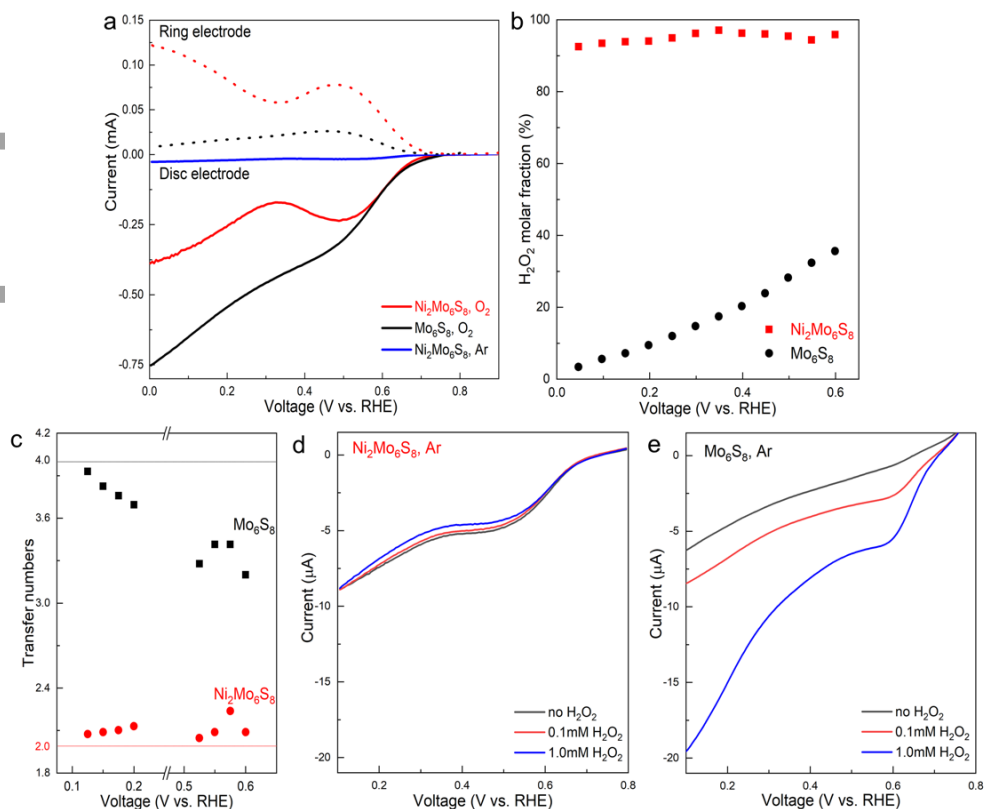


Figure 2: Selective electrochemical O₂ reduction to H₂O₂ on the Ni₂Mo₆S₈ catalyst: a) comparison of RRDE voltammograms of Ni₂Mo₆S₈ and Mo₆S₈ catalysts in O₂ and Ar saturated electrolytes (loading = 0.22 mg cm⁻², 900 rpm), the dashed lines refer to the simultaneous H₂O₂ oxidation currents at the Pt ring electrode; b) comparison of H₂O₂ molar selectivity based on ring and disc currents; c) transfer numbers based on RRDE voltammograms at different rotating rates; LSV curves of the d) Ni₂Mo₆S₈ and e) Mo₆S₈ catalyst in Ar-saturated 0.1M KOH electrolyte with different concentration of pre-added H₂O₂.

Figure 2a compares the iR-corrected linear sweep voltammograms (LSV, 5 mV/s) for Ni₂Mo₆S₈ and Mo₆S₈ in 0.1M KOH saturated with either Ar- or O₂ (flow rate: 20 sccm, pressure: ~ 800 torr). The cathodic sweep was employed for the disk electrode to avoid anodic leaching of Ni²⁺ from the catalyst. The Ni₂Mo₆S₈ catalyst exhibited an ORR onset potential of ~ 0.75V vs. RHE, which is close to the normalized thermodynamic potential of ~ 0.82V for H₂O₂ production in 0.1M KOH (assuming HO₂⁻ concentration of 1mM, O₂ pressure of 800 torr and equivalent activity coefficient for HO₂⁻ and OH⁻).^[13c] The cathodic reduction current was mainly due to the ORR as the sweep in Ar-saturated electrolyte exhibited neglectable Faradic current. Importantly, the ring current responded instantly with the onset of ORR and exhibited the same trend as the disc current. Comparison of disc and ring currents using the calibrated ring collection efficiency of 0.38 reveals nearly exclusive

formation of H_2O_2 , with H_2O_2 molar fraction higher than 90% throughout the voltage range and peaked with 98% at $\sim 0.4\text{V}$ vs. RHE (Figure 2b). The control Ni-free Mo_6S_8 catalysts, in contrast, delivered about twice higher ORR currents and the H_2O_2 molar fraction was only $\sim 40\%$ at 0.6V vs. RHE and gradually decreased to $\sim 10\%$ at 0.1V vs. RHE. As another control catalyst, we also tested the MoS_2 electrocatalyst and the general behavior is similar as Mo_6S_8 (Figure S5). We then collected RRDE voltammograms at rotating rates from 625 to 1600 rpm (Figure S6). The $\text{Ni}_2\text{Mo}_6\text{S}_8$ catalyst delivered consistently higher than 90% H_2O_2 molar selectivity at all rotating rates, and the average number of transferred electrons was estimated as $2.1\sim 2.3$ using the Koutecky-Levich equation (Figure 2c). This is in strong contrast with the Ni-free Mo_6S_8 catalyst where the H_2O_2 selectivity decreased by $\sim 10\%$ as the rotating rate was increased from 625 to 1600 rpm (Figure S7), and the average number of transfer electrons was voltage dependent and was much higher than the $\text{Ni}_2\text{Mo}_6\text{S}_8$ catalyst. This voltage and O_2 mass transfer dependent selectivity in the absence of Ni ions, in combination with the larger ORR disc current, suggest that Ni ions in $\text{Ni}_2\text{Mo}_6\text{S}_8$ play vital roles on suppressing $4e^-$ ORR and inhibit O-O cleavage for exclusive H_2O_2 synthesis.

We then verified that the $\text{Ni}_2\text{Mo}_6\text{S}_8$ catalysts are intrinsically inactive to decompose H_2O_2 and unable to catalyze a $2e^- + 2e^-$ mechanism during the ORR. Figure 2d-e compare voltammograms from the $\text{Ni}_2\text{Mo}_6\text{S}_8$ and Mo_6S_8 catalysts in Ar-saturated electrolytes with different concentrations of pre-added H_2O_2 . The small cathodic currents observed in all voltammograms were due to persist O_2 after Ar purging and the addition of H_2O_2 did not generate any increases in Faradic current for the $\text{Ni}_2\text{Mo}_6\text{S}_8$ catalyst. In fact, the current was slightly decreased due to shift in Nernstian potentials associated with higher H_2O_2 concentration as discussed in prior works.^[13c] The Mo_6S_8 catalyst, in comparison, exhibited H_2O_2 -concentration dependent Faradic currents and hence has intrinsic activity for reducing H_2O_2 to H_2O . Therefore, the comparison clearly suggests that splitting of O-O bonds appears infeasible for the $\text{Ni}_2\text{Mo}_6\text{S}_8$ catalyst, which is critical for selective H_2O_2 synthesis using the $2e^-$ ORR.

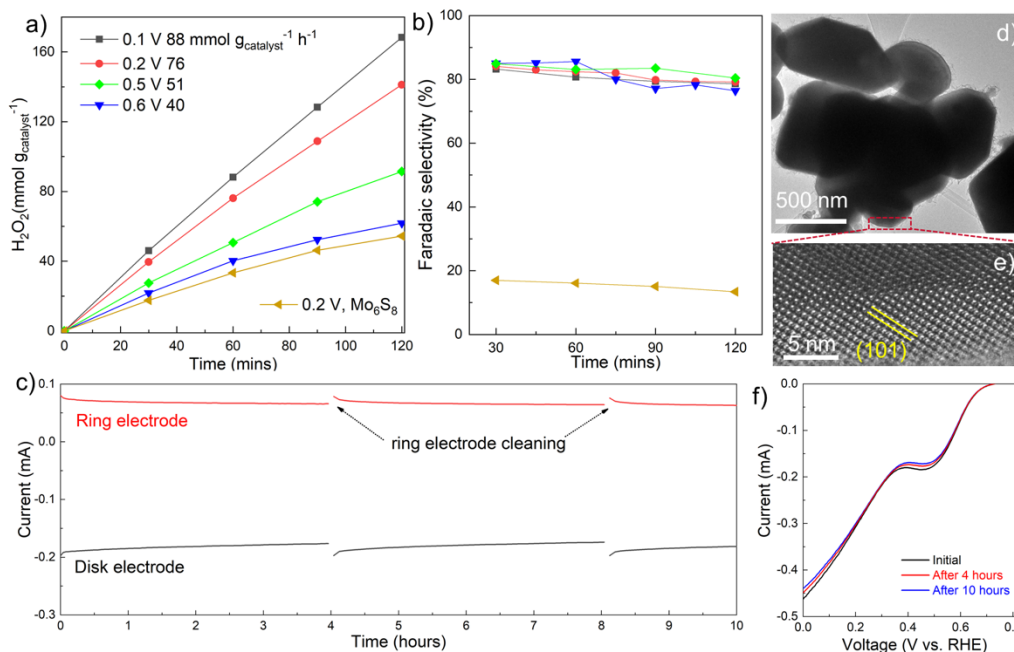


Figure 3: Electrocatalytic stability and chemical quantification of accumulated H_2O_2 : comparison of $\text{Ni}_2\text{Mo}_6\text{S}_8$ and Mo_6S_8 electrocatalysts on the basis of a) cumulative H_2O_2 yields normalized by catalyst loading and b) H_2O_2 Faradaic selectivity over reaction time at different potentials; c) evolution of Faradic currents at the ring and disk electrodes for 10 hours continuous H_2O_2 synthesis using the $\text{Ni}_2\text{Mo}_6\text{S}_8$ catalyst, d-e) post-mortem TEM analysis of $\text{Ni}_2\text{Mo}_6\text{S}_8$ catalyst; f) comparison of LSV voltammograms acquired during the stability test.

The production rates and Faradaic efficiencies for H_2O_2 synthesis on the $\text{Ni}_2\text{Mo}_6\text{S}_8$ catalyst were quantified under different potentials using the potentiostatic technique (0.22 mg cm^{-2} , 900 rpm). Of note, the Faradic ORR currents were relatively stable under all testing conditions even for the high current electrolysis at 0.1V vs. RHE (Figure S8). The electrolytes were sampled at a 30 min interval under each potential and concentration of accumulated H_2O_2 was quantified using the ceric sulfate ($\text{Ce}(\text{SO}_4)_2$) titration method as detailed in the supplementary information (Figure S9).^[10] The H_2O_2 yielding rate exhibited nearly linear relationship with regards to electrolysis duration at all voltages examined here (Figure 3a), with a rate of $40 \text{ mmol H}_2\text{O}_2 \text{ g}_{\text{cat}}^{-1} \text{ h}^{-1}$ at 0.6V vs. RHE and reached $88 \text{ g}_{\text{cat}}^{-1} \text{ h}^{-1}$ at 0.1V vs. RHE. The Faradic efficiency was estimated in reference to the total passed charge, and exceed 72% under all examined voltages and the highest was observed as 85% at 0.6V vs. RHE (Figure 3b). Of note, these Faradic efficiencies are consistent with the $\sim 92\%$ H_2O_2 molar fraction estimated from RRDE due to different calculation protocols were used (up to $\sim 17.2\%$ theoretical difference).^[25] Nevertheless, it was verified from both protocols that high H_2O_2 selectivity was obtained from a wide voltage range, suggesting $\text{Ni}_2\text{Mo}_6\text{S}_8$ should be intrinsically active for

selective H₂O₂ synthesis. The control Mo₆S₈ catalyst, in contrast, exhibited much higher ORR current under the same voltages from 0.1 to 0.5V vs. RHE and the corresponding H₂O₂ Faradic selectivity were all merely 20% (Figure S10). Therefore, these results clearly establish that H₂O₂ is the principal ORR product from the Ni₂Mo₆S₈ catalyst, making it a very promising for H₂O₂ synthesis using alkaline fuel cells.

The use of 0.22 mg cm⁻² as the optimal Ni₂Mo₆S₈ catalyst loading was based on variations of ORR current and H₂O₂ molar selectivity as the catalyst loading was increased from 0.1 to 1.5 mg cm⁻² (Figure S11). The ORR current increased with higher loadings for loadings less than 0.30 mg/cm² due to more available active sites and the H₂O₂ molar selectivity remained stable and was consistently higher than 90%. In contrast, both ORR current and H₂O₂ selectivity started to fluctuate and become inconsistent with loadings exceed 0.30 mg cm⁻². This comparison suggests that under low catalyst loadings, the available active sites are likely all saturated by O₂ and exhibited nearly exclusive H₂O₂ selectivity whereas under higher loadings a portion of unsaturated active sites perhaps triggered side reactions that compromised H₂O₂ selectivity. On the other hand, optimal Nafion content was identified as 0.23 wt.% using electrodes with the same 0.22 mg cm⁻² Ni₂Mo₆S₈ loading (Figure S12).

The stability of the Ni₂Mo₆S₈ catalyst for continuous H₂O₂ production was evaluated for 10 hours using RRDE setup at 0.5 V vs. RHE and 900 rpm (Figure 3c). The electrode was prepared with 0.80 mg/cm² Ni₂Mo₆S₈ and 8.99 wt.% Nafion loading, which although has slightly compromised H₂O₂ selectivity was necessary to ensure sufficient electrode mechanical stability as immobilizing large Ni₂Mo₆S₈ particles under vigorous O₂ bubbling and 900 rpm was challenging. The Pt ring electrode was cleaned every 4 hours to ensure sufficient activity on responding to H₂O₂. Overall, the disc current decayed from the initial 0.193 mA to 0.177 mA after 10 hours (92% retention) and the ring current decayed from the initial 0.070 mA to 0.062 mA after 10 hours (89% retention). The LSV profiles acquired during the stability test exhibited slight decays in ORR kinetic current (Figure 3f). Importantly, TEM analysis suggests that the aged catalyst had similar morphology and lattice parameter as pristine Ni₂Mo₆S₈ (Figure 3d-e). The Raman resonance peaks from aged and pristine catalysts are also similar (Figure S13). Inductively coupled plasma atomic emission spectroscopy (ICP-AAS) analysis of the electrolyte after a durability test did not show measurable Ni²⁺ concentration. These results suggest that the Ni₂Mo₆S₈ catalyst has good material stability and did not undergo severe oxidation or decomposition. The slight decay in kinetic current was likely due to mechanical instability of the electrode as detached catalyst particles were consistently observed. Further

This article is protected by copyright. All rights reserved.

optimization of electrode architecture with stronger particle to particle binding should substantially improve durability for long operations.

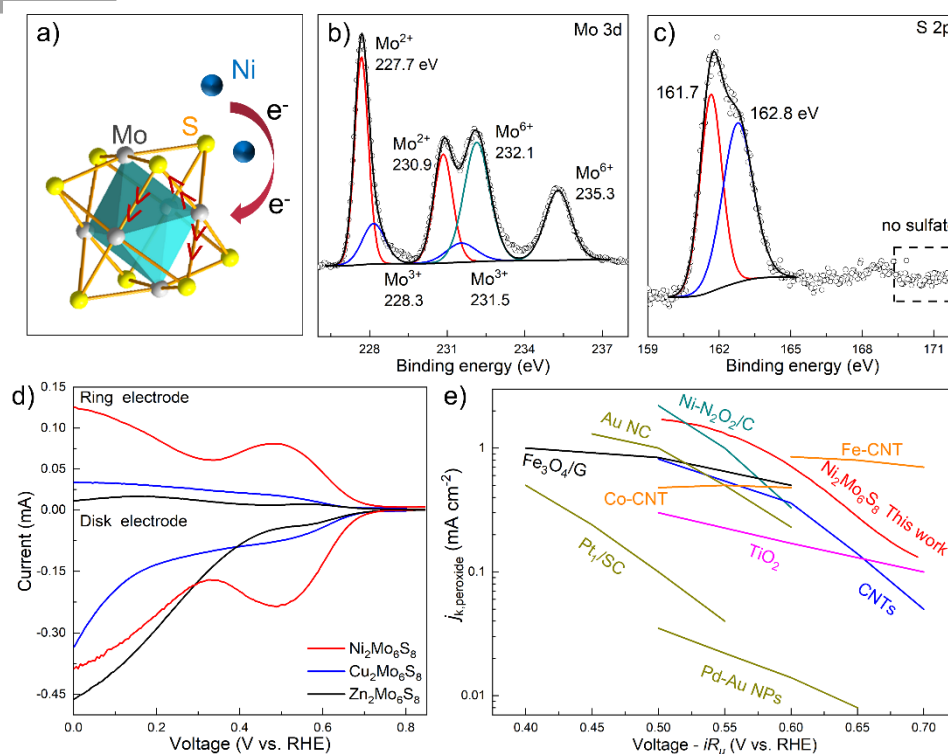


Figure 4: a) Schematic illustration of Ni-Mo₆S₈ electronic interactions in Ni₂Mo₆S₈; b) Mo 3d and c) S 2p high-resolution regional XPS spectra; d) comparison of RRDE profiles of Ni₂Mo₆S₈ with Cu₂Mo₆S₈ and Zn₂Mo₆S₈ electrocatalysts; e) comparison of mass-transport corrected kinetic current densities for H₂O₂ production on Ni₂Mo₆S₈ (1600 rpm) with literature electrocatalysts based on RRDE measurements, including acidic electrocatalysts Pt₁/SC,^[11] and Pd-Au NPs^[26]; and alkaline electrocatalysts Ni-N₂O₂/C^[27], CNTs^[9a], Fe₃O₄/G^[28], TiO₂^[29], Au NC^[30], Co-CNT and Fe-CNT.^[31]

The above results outlined that Ni ions in the Ni₂Mo₆S₈ catalyst played vital roles for highly selective 2e⁻ ORR to H₂O₂, which in reference to prior theoretical studies can be rationalized as the ligand and ensemble effects of Ni on Mo₆S₈ clusters and the spatial confinement of the Chevrel phase structure.^[32] The ligand effect refers to electron transfer from Ni to Mo₆S₈ and increase electron densities on Mo and S, which were verified with X-ray photoelectron spectroscopy analysis (XPS) that suggest Ni predominately assume the oxidized Ni²⁺ state and both Mo and S were partially reduced compared with the Mo₆S₈ catalyst (more pronounced Mo²⁺-subpeak and ~ 0.5 eV negative shift in S 2p binding energy, **Figure 4** a-c, S14-15). Such changes in electron densities enhance

This article is protected by copyright. All rights reserved.

adsorption and dissociation of the proton donor H₂O since binding energies of dissociation intermediates on Ni/Mo and S were stronger, and accelerate the proton-coupled O₂ reduction to *OOH (O₂ + * + H₂O + e⁻ → *OOH + OH⁻, * refers to active sites). The ensemble effect of Ni refers to Ni²⁺ as a key constitute of the active center motif and was revealed by comparing with the Cu₂Mo₆S₈ and Zn₂Mo₆S₈ catalysts, as both catalysts have the same Chevrel phase structure but different metal cations and delivered smaller ORR catalyst and much lower H₂O₂ selectivity (Figure 4d, S16-17). The key role of Ni²⁺ was also verified with the control NiS electrocatalyst where similar ORR kinetic current and reasonably high H₂O₂ selectivity of ~ 65% were observed at low overpotentials (Figure S18). On the other hand, the unique atomic coordination of Ni, Mo and S in the Chevrel phase enhances H₂O₂ selectivity by spatially separating nearby active Ni centers to 6.26 Å with Mo₆S₈ clusters. This distance is too large compared with the O-O distance of 1.44Å and hence is unfavorable for the binuclear O-O dissociation in *OOH. This is further supported by comparison with the NiS electrocatalyst (Ni-Ni distance 2.52 Å) where H₂O₂ selectivity quickly decreased at increased overpotentials due to accelerated O-O dissociation (Figure S18). The unfavorable O-O dissociation on the Ni₂Mo₆S₈ catalyst was also discussed in prior theoretical simulations where stabilization of *O on either Mo or Ni was unfavorable and has high energy barrier.^[32b] Overall, the synergy of these ligand, ensemble and spatial confinement effects modulate the oxygen reduction pathway toward the nearly exclusive H₂O₂ formation in alkaline electrolyte.

The mass-transport corrected kinetic current density for H₂O₂ production (j_k , H₂O₂) on the Ni₂Mo₆S₈ catalyst was estimated using the Koutecky-Levich equation and was 1.5 mA cm⁻² at 0.53 V vs. RHE, which is comparable or even better than the state-of the art nanocluster and single atom based electrocatalysts and electrocatalysts based on noble and/or toxic metals, demonstrating superior activity of Ni₂Mo₆S₈ for H₂O₂ synthesis (Figure 4e, Table S2). Furthermore, we estimated the turn-over frequency (TOF) for H₂O₂ formation by assuming Ni was the only active site and all exposed Ni₂Mo₆S₈ surface was active. The surface density of Ni active site was estimated as 1.64×10¹⁴ cm⁻² using the crystal facet model illustrated in Figure 1b (2 Ni sites per Mo₆S₈ cluster). On the basis of these assumptions and the electrochemical active surface area of Ni₂Mo₆S₈ as 1.82 m² g⁻¹ (Figure S19), the TOF for H₂O₂ formation was estimated as ~ 30 s⁻¹ and this is among the highest compared with existing catalysts even including single atom catalysts.^[13b] The high selectivity and fast TOF make the Ni-Mo₆S₈ active site motif as one of the most active non-precious electrocatalysts. Further advances on materials synthesis using novel precursors or structural templates that target Ni₂Mo₆S₈ nanoclusters may significantly accelerate the development of such catalysts. The results

This article is protected by copyright. All rights reserved.

presented here provide new design principles for rational active sites motifs with earth abundant elements for sustainable and decentralized H₂O₂ production.

Conclusion

In summary, we demonstrate the Chevrel phase chalcogenide Ni₂Mo₆S₈ as a new Earth-abundant catalyst for tuning electrocatalytic oxygen reduction specifically toward synthesizing H₂O₂. The Ni₂Mo₆S₈ catalyst has unique active center motif that invokes synergistic ligand, ensemble and spatial effects between Ni and Mo₆S₈, which provides optimal binding with key reaction intermediates and effectively resists the undesirable O-O scission, leading to fast turn-over frequency for selective H₂O₂ synthesis in aqueous electrolytes. Both RRDE and chemical titration measurements confirm that the novel Ni₂Mo₆S₈ catalyst provides highly efficient H₂O₂ production with > 90% molar selectivity at a wide potential range and a high yielding rate of ~ 90 mmol H₂O₂ g_{cat}⁻¹ h⁻¹ despite of its very low surface area. This identification of Ni-Mo₆S₈ as a new type of noble-metal free active center motif for tuning oxygen reduction may unlock new opportunities in the search of practical catalysts for onsite decentralized production of low cost hydrogen peroxide.

Supporting Information

Supporting Information is available from the Wiley Online Library or from the author.

Acknowledgements

This work is supported by startup grants from Northern Illinois University. Use of the Center for Nanoscale Materials, an Office of Science user facility, was supported by the U.S. Department of

This article is protected by copyright. All rights reserved.

Energy, Office of Science, Office of Basic Energy Sciences, under Contract No. DE-AC02-06CH11357. We also thank the support provided by the U.S. Department of Energy, Office of Science, Office of Basic Energy Sciences under Award Number DOE DE-FG02-03ER15457 to the Institute for Catalysis in Energy Processes (ICEP) at Northwestern U (Y.L., T.J.M). This work made use of the Keck-II facility of Northwestern University's NUANCE Center, which has received support from the SHyNE Resource (NSF ECCS-2025633), the IIN, and Northwestern's MRSEC program (NSF DMR-1720139). Argonne National Laboratory's contribution is based upon work supported by Laboratory Directed Research and Development (LDRD) funding from Argonne National Laboratory, provided by the Director, Office of Science, of the U.S. Department of Energy.

Received: ((will be filled in by the editorial staff))

Revised: ((will be filled in by the editorial staff))

Published online: ((will be filled in by the editorial staff))

References

- [1] a) S. Siahrostami, S. J. Villegas, A. H. Bagherzadeh Mostaghimi, S. Back, A. B. Farimani, H. Wang, K. A. Persson, J. Montoya, *ACS Catal.* **2020**, *10*, 7495; b) J. M. Campos-Martin, G. Blanco-Brieva, J. L. Fierro, *Angew. Chem. Int. Ed.* **2006**, *45*, 6962.
- [2] R. Ciriminna, L. Albanese, F. Meneguzzo, M. Pagliaro, *ChemSusChem* **2016**, *9*, 3374.
- [3] K. Jiang, J. Zhao, H. Wang, *Adv. Funct. Mater.* **2020**, *30*, 2003321.
- [4] R. J. Lewis, G. J. Hutchings, *ChemCatChem* **2019**, *11*, 298.
- [5] a) N. M. Wilson, D. W. Flaherty, *J. Am. Chem. Soc.* **2016**, *138*, 574; b) K. Dong, Y. Lei, H. Zhao, J. Liang, P. Ding, Q. Liu, Z. Xu, S. Lu, Q. Li, X. Sun, *J. Mater. Chem. A* **2020**, *8*, 23123.
- [6] J. K. Edwards, G. J. Hutchings, *Angew. Chem. Int. Ed.* **2008**, *47*, 9192.

This article is protected by copyright. All rights reserved.

- [7] a) Y. Sun, L. Han, P. Strasser, *Chem. Soc. Rev.* **2020**, *49*, 6605; b) J. Zhang, H. Zhang, M.-J. Cheng, Q. Lu, *Small* **2020**, *16*, 1902845.
- [8] a) S. C. Perry, D. Pangotra, L. Vieira, L.-I. Csepei, V. Sieber, L. Wang, C. Ponce de León, F. C. Walsh, *Nat. Rev. Chem.* **2019**, *3*, 442; b) K. Dong, J. Liang, Y. Wang, Z. Xu, Q. Liu, Y. Luo, T. Li, L. Li, X. Shi, A. M. Asiri, Q. Li, D. Ma, X. Sun, *Angew. Chem. Int. Ed.* **2021**, *60*, 10583.
- [9] a) Z. Lu, G. Chen, S. Siahrostami, Z. Chen, K. Liu, J. Xie, L. Liao, T. Wu, D. Lin, Y. Liu, T. F. Jaramillo, J. K. Nørskov, Y. Cui, *Nat. Catal.* **2018**, *1*, 156; b) C. Xia, S. Back, S. Ringe, K. Jiang, F. Chen, X. Sun, S. Siahrostami, K. Chan, H. Wang, *Nat. Catal.* **2020**, *3*, 125.
- [10] B. Q. Li, C. X. Zhao, J. N. Liu, Q. Zhang, *Adv. Mater.* **2019**, *31*, e1808173.
- [11] C. H. Choi, M. Kim, H. C. Kwon, S. J. Cho, S. Yun, H.-T. Kim, K. J. J. Mayrhofer, H. Kim, M. Choi, *Nat. Commun.* **2016**, *7*, 10922.
- [12] a) J. S. Jirkovský, I. Panas, E. Ahlberg, M. Halasa, S. Romani, D. J. Schiffrin, *J. Am. Chem. Soc.* **2011**, *133*, 19432; b) A. Verdager-Casadevall, D. Deiana, M. Karamad, S. Siahrostami, P. Malacrida, T. W. Hansen, J. Rossmeisl, I. Chorkendorff, I. E. L. Stephens, *Nano Lett.* **2014**, *14*, 1603.
- [13] a) C. Tang, Y. Jiao, B. Shi, J. N. Liu, Z. Xie, X. Chen, Q. Zhang, S. Z. Qiao, *Angew. Chem. Int. Ed.* **2020**, *59*, 9171; b) E. Jung, H. Shin, B. H. Lee, V. Efremov, S. Lee, H. S. Lee, J. Kim, W. Hooch Antink, S. Park, K. S. Lee, S. P. Cho, J. S. Yoo, Y. E. Sung, T. Hyeon, *Nat. Mater.* **2020**, *19*, 436; c) H. W. Kim, M. B. Ross, N. Kornienko, L. Zhang, J. Guo, P. Yang, B. D. McCloskey, *Nat. Catal.* **2018**, *1*, 282; d) T. P. Fellinger, F. Hasche, P. Strasser, M. Antonietti, *J. Am. Chem. Soc.* **2012**, *134*, 4072; e) Y. Pang, K. Wang, H. Xie, Y. Sun, M.-M. Titirici, G.-L. Chai, *ACS Catal.* **2020**, *10*, 7434; f) Z. Xu, H. Zhao, J. Liang, Y. Wang, T. Li, Y. Luo, X. Shi, S. Lu, Z. Feng, Q. Wu, X. Sun, *Mater. Today Phys.* **2020**, *15*, 100280.

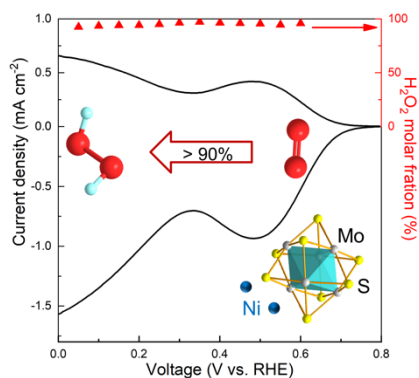
- [14] Y. Sun, I. Sinev, W. Ju, A. Bergmann, S. Dresp, S. Kühl, C. Spöri, H. Schmies, H. Wang, D. Bernsmeier, B. Paul, R. Schmack, R. Kraehnert, B. Roldan Cuenya, P. Strasser, *ACS Catal.* **2018**, *8*, 2844.
- [15] a) H. Sheng, E. D. Hermes, X. Yang, D. Ying, A. N. Janes, W. Li, J. R. Schmidt, S. Jin, *ACS Catal.* **2019**, *9*, 8433; b) H. Sheng, A. N. Janes, R. D. Ross, D. Kaiman, J. Huang, B. Song, J. R. Schmidt, S. Jin, *Energy Environ. Sci.* **2020**, *13*, 4189; c) L. Zhang, J. Liang, L. Yue, Z. Xu, K. Dong, Q. Liu, Y. Luo, T. Li, X. Cheng, G. Cui, B. Tang, A. A. Alshehri, K. A. Alzahrani, X. Guo, X. Sun, *Nano Res.* **2021**, <https://doi.org/10.1007/s12274-021-3474-0>.
- [16] R. Gao, L. Pan, Z. Li, C. Shi, Y. Yao, X. Zhang, J.-J. Zou, *Adv. Funct. Mater.* **2020**, *30*, 1910539.
- [17] a) A. Izgorodin, E. Izgorodina, D. R. MacFarlane, *Energy Environ. Sci.* **2012**, *5*; b) M. Wang, N. Zhang, Y. Feng, Z. Hu, Q. Shao, X. Huang, *Angew. Chem. Int. Ed.* **2020**, *59*, 14373.
- [18] a) S. Siahrostami, A. Verdaguer-Casadevall, M. Karamad, D. Deiana, P. Malacrida, B. Wickman, M. Escudero-Escribano, E. A. Paoli, R. Frydendal, T. W. Hansen, I. Chorkendorff, I. E. L. Stephens, J. Rossmeisl, *Nat. Mater.* **2013**, *12*, 1137; b) J. Liang, Y. Wang, Q. Liu, Y. Luo, T. Li, H. Zhao, S. Lu, F. Zhang, A. M. Asiri, F. Liu, D. Ma, X. Sun, *J. Mater. Chem. A* **2021**, *9*, 6117; c) C. Tang, Y. Jiao, B. Shi, J.-N. Liu, Z. Xie, X. Chen, Q. Zhang, S.-Z. Qiao, *Angew. Chem. Int. Ed.* **2020**, *59*, 9171.
- [19] a) J. Jiang, M. Gao, W. Sheng, Y. Yan, *Angew. Chem. Int. Ed.* **2016**, *55*, 15240; b) K. Lilova, J. T. Perryman, N. R. Singstock, M. Abramchuk, T. Subramani, A. Lam, R. Yoo, J. C. Ortiz-Rodríguez, C. B. Musgrave, A. Navrotsky, J. M. Velázquez, *Chem. Mater.* **2020**, *32*, 7044.
- [20] K. Lu, Y. Liu, J. Chen, Z. Zhang, Y. Cheng, *ACS Nano* **2019**, *13*, 14540.
- [21] E. Levi, D. Aurbach, *Chem. Mater.* **2010**, *22*, 3678.

- [22] M. Mao, Z. Lin, Y. Tong, J. Yue, C. Zhao, J. Lu, Q. Zhang, L. Gu, L. Suo, Y.-S. Hu, H. Li, X. Huang, L. Chen, *ACS Nano* **2020**, *14*, 1102.
- [23] Y. Cheng, L. R. Parent, Y. Shao, C. Wang, V. L. Sprenkle, G. Li, J. Liu, *Chem. Mater.* **2014**, *26*, 4904.
- [24] X. Tan, H. A. Tahini, S. C. Smith, *Mater. Horizons* **2019**, *6*, 1409.
- [25] C. Xia, J. Y. Kim, H. Wang, *Nat. Catal.* **2020**, *3*, 605.
- [26] E. Pizzutilo, O. Kasian, C. H. Choi, S. Cherevko, G. J. Hutchings, K. J. J. Mayrhofer, S. J. Freakley, *Chem. Phys. Lett.* **2017**, *683*, 436.
- [27] Y. Wang, R. Shi, L. Shang, G. I. N. Waterhouse, J. Zhao, Q. Zhang, L. Gu, T. Zhang, *Angew. Chem. Int. Ed.* **2020**, *59*, 13057.
- [28] W. R. P. Barros, Q. Wei, G. Zhang, S. Sun, M. R. V. Lanza, A. C. Tavares, *Electrochim. Acta* **2015**, *162*, 263.
- [29] M. A. Ghanem, A. M. Al-Mayouf, M. N. Shaddad, F. Marken, *Electrochim. Acta* **2015**, *174*, 557.
- [30] Y. Lu, Y. Jiang, X. Gao, W. Chen, *ChemComm* **2014**, *50*, 8464.
- [31] K. Jiang, S. Back, A. J. Akey, C. Xia, Y. Hu, W. Liang, D. Schaak, E. Stavitski, J. K. Nørskov, S. Siahrostami, H. Wang, *Nat. Commun.* **2019**, *10*, 3997.
- [32] a) C. Liu, P. Liu, *ACS Catalysis* **2015**, *5*, 1004-1012; b) H. T. Zhang, C. Liu, P. Liu, Y. H. Hu, *J. Chem. Phys.* **2019**, *151*, 024304.

A new active site motif based on Chevrel phase $\text{Ni}_2\text{Mo}_6\text{S}_8$ for electrochemical synthesis of H_2O_2 with $\sim 98\%$ molar selectivity. The activity originates from ligand and ensemble effects of Ni that promote H_2O dissociation and O_2 reduction to HOO^* , and spatial effect that isolates active sites and inhibits O-O cleavage. The catalyst exhibited a high turn-over frequency of $\sim 30\text{s}^{-1}$ and H_2O_2 production rate of $90\text{ mmol g}_{\text{cat}}^{-1}\text{h}^{-1}$.

Fan Xia, Bomin Li, Yiqi Liu, Yuzi Liu, Siyuan Gao, Ke Lu, Jacob Kaelin, Rongyue Wang, Tobin J. Marks, and Yingwen Cheng*

Carbon Free and Noble Metal Free $\text{Ni}_2\text{Mo}_6\text{S}_8$ Electrocatalyst for Selective Electrosynthesis of H_2O_2



This article is protected by copyright. All rights reserved.

Author Manuscript